Solar Phys (2017) 292:125
DOI 10.1007/s11207-017-1147-7

Earth-Affecting Coronal Mass Ejections Without Obvious Low Coronal Signatures

Nariaki V. Nitta[1] · **Tamitha Mulligan**[2]

Received: 16 February 2017 / Accepted: 20 July 2017

Abstract We present a study of the origin of coronal mass ejections (CMEs) that were not accompanied by obvious low coronal signatures (LCSs) and yet were responsible for appreciable disturbances at 1 AU. These CMEs characteristically start slowly. In several examples, extreme ultraviolet (EUV) images taken by the *Atmospheric Imaging Assembly* onboard the *Solar Dynamics Observatory* reveal coronal dimming and a post-eruption arcade when we make difference images with long enough temporal separations, which are commensurate with the slow initial development of the CME. Data from the EUV imager and COR coronagraphs of the *Sun Earth Connection Coronal and Heliospheric Investigation* onboard the *Solar Terrestrial Relations Observatory*, which provide limb views of Earth-bound CMEs, greatly help us limit the time interval in which the CME forms and undergoes initial acceleration. For other CMEs, we find similar dimming, although only with lower confidence as to its link to the CME. It is noted that even these unclear events result in unambiguous flux rope signatures in *in situ* data at 1 AU. There is a tendency that the CME source regions are located near coronal holes or open field regions. This may have implications for both the initiation of the stealthy CME in the corona and its outcome in the heliosphere.

Keywords Coronal mass ejections · Coronal holes · Extreme Ultraviolet emission · Geomagnetic storms

Earth-affecting Solar Transients
Guest Editors: Jie Zhang, Xochitl Blanco-Cano, Nariaki Nitta, and Nandita Srivastava

✉ N.V. Nitta
nitta@lmsal.com

T. Mulligan
Tamitha.M.Skov@aero.org

[1] Lockheed Martin Solar and Astrophysics Laboratory, Department A021S, Building 252, 3251 Hanover Street, Palo Alto, CA 94304, USA

[2] Space Sciences Department, The Aerospace Corporation, Los Angeles, CA 94305, USA

Published online: 28 August 2017

1. Introduction

Intense non-recurrent geomagnetic storms represent a major concern in operational space weather. They are usually attributable to coronal mass ejections (CMEs) (see, for example, Gosling, 1993). This link has been made considerably stronger since 1996 by the data from the *Large Angle and Spectrometric Coronagraph* (LASCO) onboard the *Solar and Heliospheric Observatory* (SOHO), which provides an uninterrupted view of outflows (including CMEs) from the solar corona, imaged in white light that is scattered from electron density structures. Thanks to its high sensitivity and large field of view of up to 30 $R_{\odot}$, LASCO allows us to routinely find and track Earth-bound CMEs, which are generally harder to observe than CMEs ejected above the limbs of the Sun because the cross sections of Thomson scattering are smaller for the objects that move away from the plane of the sky (*e.g.* Billings, 1966). In some cases, these CMEs may either fully or partially encompass the occultation disk, and they are accordingly called full or partial halo CMEs (Howard *et al.*, 1982; Webb *et al.*, 2000).

There were 90 intense geomagnetic storms in Solar Cycle 23 as defined by the minimum disturbance storm time (Dst) index of ≤ -100 nT (Echer *et al.*, 2008). Zhang *et al.* (2007) studied 88 of these storms (except for the two that occurred in 2006). A total of 77 geomagnetic storms involved an interplanetary coronal mass ejection (ICME) (see Zurbuchen and Richardson, 2006, for the definitions), while the remaining 11 storms appeared to result from a corotating interaction region (CIR) (Richardson *et al.*, 2006), which forms when a high-speed stream (HSS) from a coronal hole (CH) takes over a slow solar wind. For the 77 ICMEs, Zhang *et al.* (2007) found at least a partial halo CME that had angular width $\geq 110^{\circ}$ within a reasonable time range before the arrival of the ICME, as set by the observed solar wind speed. They also studied where these halo CMEs came from, using the known proxies for CMEs (*e.g.* Hudson and Cliver, 2001; Ma *et al.*, 2010; Nitta *et al.*, 2014), such as filament eruptions, coronal dimming, post-eruption arcades, and coronal waves, such as found in images from the *Extreme-ultraviolet Imaging Telescope* (EIT) onboard SOHO and the *Soft X-ray Telescope* (SXT) onboard *Yohkoh*.

For most of the CMEs, it was possible to determine the source region. However, this could not be unambiguously determined for nine ($\approx 12\%$) CMEs because apparently no CME proxies existed. This is problematic in various ways. Without low coronal signatures (LCSs), the selected halo CME could in fact have originated from the far side of the Sun, meaning that the ICME and geomagnetic storm resulted from another CME that was not observed by LASCO for whatever reason. The presence of such CMEs could also cast doubt on the ICME–CME pairs found for other events. Last, without knowing where the CME comes from, it is not possible to understand or predict the strong southward magnetic field in and around an ICME at 1 AU. This is a critical element that determines the magnitude of the geomagnetic storm (*e.g.* Tsurutani *et al.*, 1992).

The ambiguity of the frontside or backside origin of halo CMEs has been considerably ameliorated, thanks to the additional views of CMEs provided by the *Solar Terrestrial Relations Observatory* (STEREO: Kaiser *et al.*, 2008). STEREO consists of twin spacecraft that orbit the Sun slightly inside and outside the Earth orbit, and drift by about 22° a year in opposite directions from the Sun–Earth line. Robbrecht, Patsourakos, and Vourlidas (2009) presented the first example of a frontside CME without LCSs as observed by STEREO. The event, first detected in coronagraph data on 1 June 2008, appeared as a highly diffuse halo CME on STEREO-B (25° east of the Sun–Earth line) and a slowly developing but otherwise normal CME from the east limb on STEREO-A (28° west of the Sun–Earth line). Although EUV images from STEREO-A showed a minor prominence eruption over the east limb,

those from STEREO-B revealed no traces of the CME around the region that was thought to host it. Ma *et al.* (2010) conducted a systematic survey of CMEs during the first eight months of 2009 while the separation of STEREO was close to 90°, and found that about one-third (11/34) were stealth CMEs without LCSs on the disk. They were typically slow (*e.g.* below 300 km s^{-1}) CMEs, as in an earlier event (Robbrecht, Patsourakos, and Vourlidas, 2009).

The failure to detect the LCSs of CMEs may result from the limited sensitivity and temperature response of the observing instrument (Howard and Harrison, 2013). This possibility can be addressed with data from the *Atmospheric Imaging Assembly* (AIA: Lemen *et al.*, 2012) onboard the *Solar Dynamics Observatory* (SDO: Pesnell, Thompson, and Chamberlin, 2012). Since 2010, AIA has been taking full-disk images of the Sun at an unprecedented 12-second cadence in seven EUV channels that cover a broad range of temperature. The primary purpose of this article is to present AIA observations of Earth-affecting CMEs whose LCSs are elusive in standard data-analysis settings. In order to constrain the time range of CME formation and acceleration, we also use data, when available, from the *Sun Earth Connection Coronal and Heliospheric Investigation* (SECCHI: Howard *et al.*, 2008) on STEREO. In the next section, we briefly review our present understanding of CMEs without clear LCSs and their possible heliospheric consequences. As an example of a stealthy but geoeffective event, we feature the 5 October 2012 CME in Section 3. This event is not as stealthy as other CMEs, but the LCSs are quite weak, nonetheless. In Section 4 we discuss other non-standard CMEs and ICMEs whose solar origins are harder to understand. It appears that the source regions of these stealthy CMEs tend to be close to CHs or open field regions. The results of our analysis are discussed in Section 5 and summarized in Section 6.

2. Stealthy CMEs: Why Do We Care?

As a pathway to reliable and useful space weather prediction in the future, it is important to establish a solid link between geomagnetic storms, or more broadly speaking, ICMEs at 1 AU, and eruptive phenomena that start on the Sun. The following examples from our experience illustrate the difficulty to do this. First, a CME occurs and the source region is clearly identified on the side of the Sun that faces the observer, but it is not observed as an ICME at a later time. Perhaps the CME may not survive to 1 AU or it may be significantly deflected. Second, an ICME is observed at 1 AU, but there is no CME near the Sun within a reasonable time window. The parent CME may be too diffuse to be observed by coronagraphs with finite sensitivity. It could be diffuse from the outset or become more diffuse before it emerges above the coronagraph occultation disk in the plane of the sky. There is also the possibility that the CME may be still ill-formed even at several solar radii from the Sun. Third, there are multiple CMEs preceding a single ICME, and it is not clear which one is responsible for the ICME. Multiple CMEs, perhaps through CME–CME interaction, could also contribute to the ICME. Last, when a CME is observed near the Sun that accounts for the ICME, we may not see its signatures in the low corona. This is often the case for a slow CME.

The last problem is well represented in the 1 – 2 June 2008 CME mentioned earlier (Robbrecht, Patsourakos, and Vourlidas, 2009), even though it was directed toward STEREO-B rather than the Earth. Following this event, the term "stealth CME"[1] has been in wide use, which may implicitly indicate a class of CMEs distinct from other CMEs associated with a flare and/or filament eruption. The event studied by Robbrecht, Patsourakos, and

[1] CMEs that apparently lack the associated near-surface activity were known even from the *Skylab* observations, and called "spontaneous CMEs" (Wagner, 1984).

Vourlidas (2009) also appeared to be a "streamer blowout" CME (Sheeley *et al.*, 1982; Howard *et al.*, 1985), which has also been considered by some researchers as a distinct class. It starts with gradual swelling and brightening of a pre-existing streamer. Howard and Harrison (2013), however, cautioned that stealth CMEs may be a product of instrument sensitivity and bandwidth issues, and proposed that they may be a low-energy end of a continuous spectrum of events that could be explained by a single mechanism or process. This latter point is supported by advanced numerical simulations of streamer blowout CMEs (van der Holst *et al.*, 2009; Lynch *et al.* 2010, 2016). As argued by Robbrecht, Patsourakos, and Vourlidas (2009), the primary discriminator for their stealth CME may be a large initiation height. These authors also suggested that the CME in question originated from a filament channel.

Subsequent case studies of stealth CMEs (Vourlidas *et al.*, 2011; Pevtsov, Panasenco, and Martin, 2012) also indicated their origins in filament channels aligned with polarity inversion lines (PILs), even though this applies to many CMEs in general and may not necessarily distinguish stealth CMEs in particular. In addition, ensemble studies (Ma *et al.*, 2010; D'Huys *et al.*, 2014) confirmed that stealth CMEs tend to be slow. D'Huys *et al.* (2014) also noted the tendency of stealth CMEs to occur close to CHs or open field regions. Another statistical study (Wang *et al.*, 2011) claimed that $\approx 16\%$ of CMEs during 1997 – 1998 may not have been detected by EIT, which is compared to the frequency of stealth CMEs of about one-third in 2009 (Ma *et al.*, 2010). After these studies, it is still an open question whether stealth CMEs can be essentially explained by the "standard model" (Svestka and Cliver, 1992) that was developed for eruptive flares.

In addition to this intriguing solar physics question, we should not discount the importance of stealth CMEs in space weather. They can cause intense geomagnetic storms, if not super storms (Kilpua *et al.*, 2014). The lack of LCSs apparently challenges space weather prediction, especially since it is not possible to identify the magnetic field structure that erupts, without knowing the source location. If we do not know the magnetic structure that erupts, how can we predict the orientation of the magnetic field in the solar wind, and specifically in the ICME, that comes in contact with the magnetosphere? The prediction of geospace impacts of these events may be challenging also because slow CMEs tend to be more strongly affected by solar wind structures and preceding CMEs (Liu *et al.*, 2016). Our primary concern is indeed in connecting heliospheric disturbances to weak CMEs that do not leave clear LCSs. Whether or not they are strictly stealth CMEs, we refer to them as being stealthy, acknowledging that the apparent lack of LCSs can at least partly be an instrumental effect (Howard and Harrison, 2013).

3. The Earth-affecting CME on 5 October 2012

Starting on 8 October 2012, there was an intense geomagnetic storm that involved an ICME. This is included in all of the *Wind* ICME Catalog,[2] the University of Science and Technology of China (USTC) List of Interplanetary Coronal Mass Ejections,[3] the Richardson and Cane Catalog of the Near-Earth Interplanetary Coronal Mass Ejections Since January 1996,[4] and

[2] http://wind.nasa.gov/ICMEindex.php. See Nieves-Chinchilla *et al.* (2017).

[3] http://space.ustc.edu.cn/dreams/wind_icmes. See Chi *et al.* (2016).

[4] http://www.srl.caltech.edu/ACE/ASC/DATA/level3/icmetable2.htm. See Cane and Richardson (2003) and Richardson and Cane (2010).

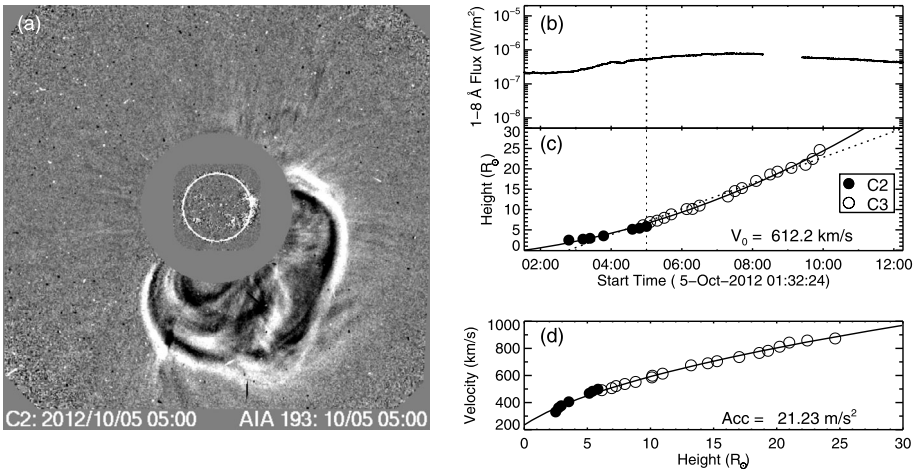

Figure 1 Partial halo CME on 5 October 2012. This is the only CME that can be linked to the geomagnetic storm three days later. (**a**) LASCO C2 difference image with the central part replaced with a contemporaneous AIA difference image. The *white circle* indicates the solar disk. (**b**) GOES soft X-ray (1 – 8 Å) light curve during an interval in which the CME was seen by LASCO. (**c**) Heliocentric height *vs.* time plot, with linear (quadratic) fits shown as the *dotted* (*solid*) *line*. The *vertical dotted line* in (**b**) and (**c**) refers to the time of the CME image in (**a**). (**d**) Velocity of the CME as calculated from the quadratic fit. All the *panels* are taken or reproduced from materials at http://cdaw.gsfc.nasa.gov.

the George Mason University CME/ICME List.[5] During 2 – 6 October, we find only one (partial) halo CME that could be responsible for the ICME, so the CME–ICME link is clear. The CME was first seen to emerge from the southwest in the LASCO image of 02:48 UT on 5 October. Figure 1a shows the CME as it approached the edge of the field of view of the C2 coronagraph. This was arguably deemed to be a stealth CME by several scientists on the International Study of Earth-affecting Solar Transient (ISEST),[6] one of the four elements of the Variability of the Sun and Its Terrestrial Impact (VarSITI) program under the Scientific Committee on Solar Terrestrial Physics (SCOSTEP).

The CME was seen to accelerate slowly, as shown in Figures 1c and d, meaning that it could have left the Sun earlier than expected from the linear extrapolation of the height-time curve (*i.e.* 02:16 UT at 1.0 $R_\odot$). Possible source regions were indeed searched for in a nearly 20-hour window before the first detection of the CME by LASCO. Figure 2 shows three examples of the proposed source regions, where some transient changes were noted. In the third example (Figures 2e and f), there seem to be subtle changes in a larger area marked with dotted ovals in cyan in addition to the region originally noted. All of these were relatively minor changes. More importantly, as shown below, they occurred much earlier than the CME initial acceleration phase, during which we expect the corona to be most strongly disturbed. Therefore they were not direct manifestations of the CME. Instead, we may speculate that they somehow contributed to destabilizing the actual CME source region.

STEREO/SECCHI observations help us narrow down the time at which the CME formed and underwent initial acceleration as shown in Figure 3. Around the time of the CME, STEREO-B and STEREO-A were located at 118° east and 125° west of the Sun–Earth

[5] http://solar.gmu.edu/heliophysics/index.php/GMU_CME/ICME_List. See Hess and Zhang (2017).

[6] See http://solar.gmu.edu/heliophysics/index.php/10/08/2012_05:00:00_UTC and Webb and Nitta (2017).

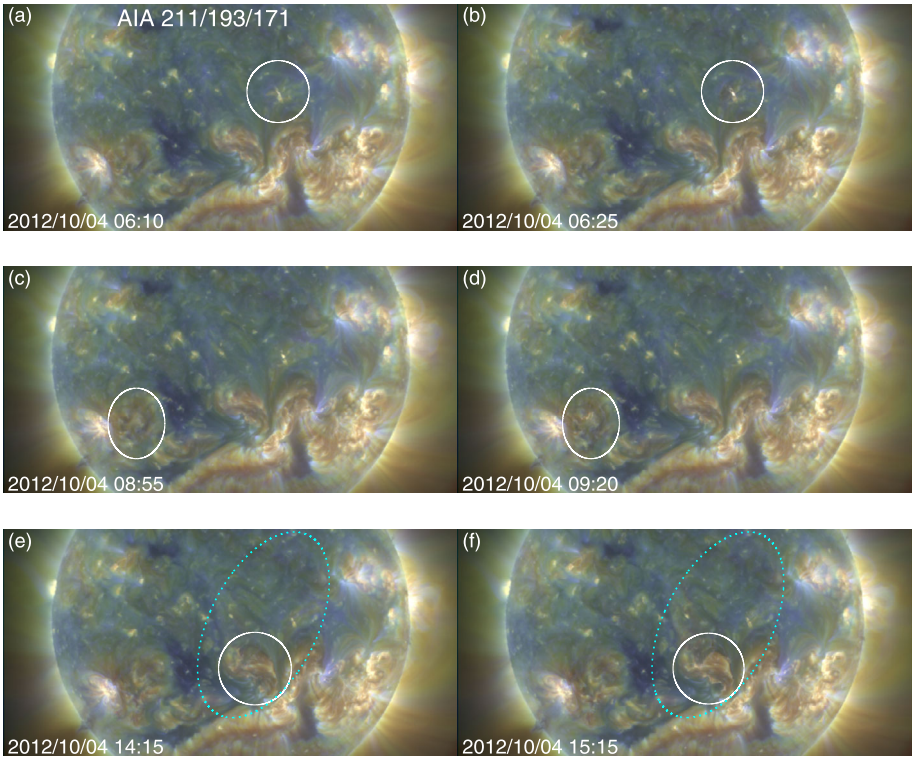

Figure 2 AIA 211-193-171 Å composite images around the times of the changes in three regions encircled in *white* that some ISEST scientists thought could be related to the CME on 5 October in Figure 1. We note subtle changes in a larger region in (**e**) and (**f**) as indicated by *dotted ovals* in *cyan*.

line (see the inset in panel (a)), respectively. In this event, the CME was seen to form in the field of view of SECCHI/COR1, which is (1.4 – 4.0) $R_{\odot}$ from Sun center. The basic cadence of COR1 was 5.0 minutes. In Figures 3a and b, we show data from COR1-B and COR1-A, respectively. They are difference images with an image five minutes earlier subtracted, although the CME is clearly seen even in the original intensity images. It looks broader from STEREO-A than from STEREO-B. Incidentally, the CME was not a classic streamer blowout – it was seen to start in COR1 images without clearly involving preexisting streamers. In Figures 3c and d we show distance (height) *vs.* time plots, which are made by measuring the signals in the radial directions, as indicated by the red rectangles in Figures 3a and b. We averaged the signals in nine pixels perpendicular to the radial directions. Based on these plots, the CME started accelerating only after 00:00 UT on 5 October. This is consistent with an impression from viewing the images as a movie. Between 00:30 and 03:00 UT, the speed of the front increased from ≈ 10 km s^{-1} to ≈ 100 km s^{-1}. We expect the LCSs to become more pronounced during and after this time range.

In Figure 4 we show AIA 211 Å images taken at 19:00 UT on 4 October and at 05:00 UT on 5 October in the upper panels. They show several active regions as bright features. There are also dark CH regions on the disk. In the lower panels, we show the percent difference $((I(t) - I(t - \delta t))/I(t - \delta t) \times 100)$ of the images in the upper panels, from which those taken five hours earlier are subtracted. We rotate the earlier image to the time of the image

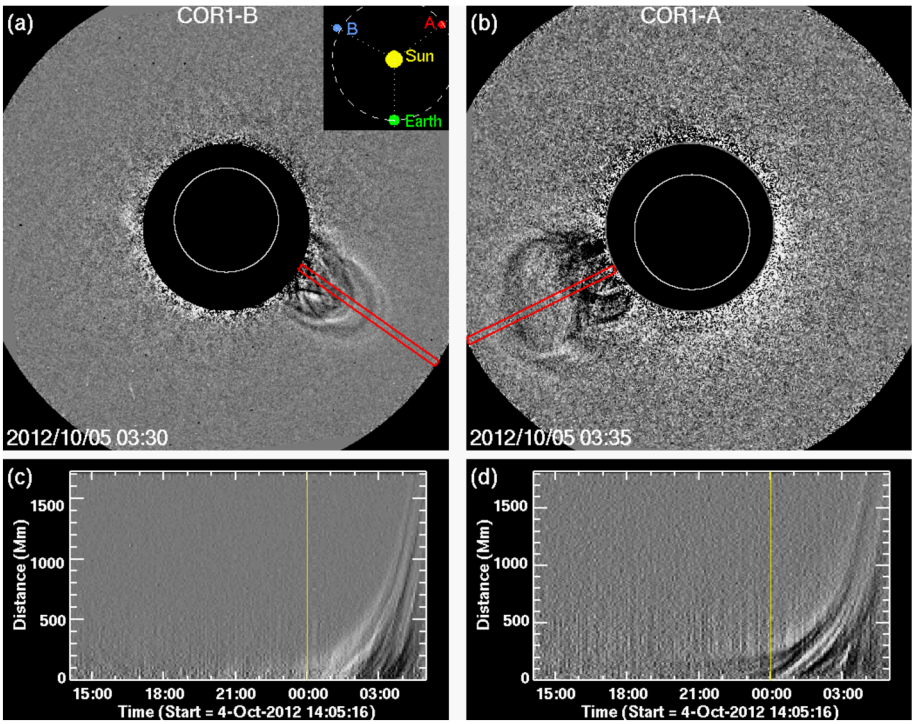

Figure 3 CME on 5 October 2010 as observed by STEREO/COR1. (**a**), (**b**) Difference images from COR1 on STEREO. The CME is tracked in the radial directions indicated in *red* in (**a**) for STEREO-B and (**b**) for STEREO-A, yielding the height *vs.* time plots shown in (**c**) and (**d**), respectively. Signals are averaged in nine pixels perpendicular to the radial directions. The locations of STEREO around the time of the CME are shown in the *inset* in (**a**).

in question, assuming the differential rotation at the photosphere. A bright region near the disk center is seen in Figure 4c, which partly overlaps with the larger area encircled in Figures 2e and f. This is too early for the CME, however. Instead, we note a slowly and steadily developing dimming in the southwest quadrant in difference images after $\approx$02:00 UT on 5 October with large time differences (*e.g.* $\delta t \geq 1$ hour). Figure 4d is an example. Between the two dimming regions, encircled in cyan in Figures 4b and d, we note a region that became brighter, which likely represented a post-eruption arcade (PEA). In AIA coronal images, this pattern was also seen in 193 Å and 335 Å images, but not in 171 Å images, suggesting that these changes occurred primarily at temperatures above ≈ 1.5 MK. The western dimming region was close to NOAA active region (AR) 11584, which showed sunspots during 1 – 6 October, peaking on 2 October with an area of 40 millionth of the solar hemisphere (MSH) and in β configuration. By 5 October, the AR decayed to 10 MSH and became simplified to an α configuration.

The PEA and dimming regions in the southwestern quadrant, with an average location at S25 W15, probably are the LCSs of the CME that puzzled the scientists on the ISEST element. The proposed earlier changes in coronal structures (see Figure 2) may have indirectly contributed to triggering the eruption, which occurred only around these LCSs after $\approx$00:00 UT on 5 October. In addition, as in Figure 1b, the GOES 1 – 8 Å soft X-ray light curve reveals a very gradual flare that peaked at B7.6 (7.6×10^{-7} W m^{-2}). Other slow and

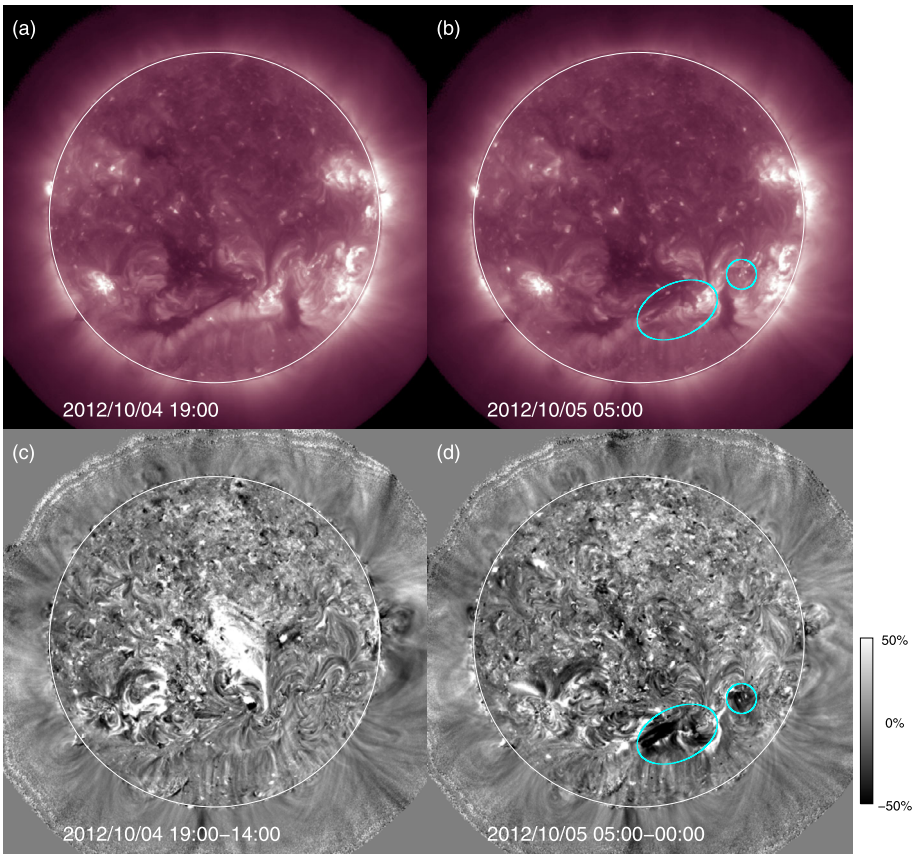

Figure 4 AIA 211 Å intensity and percent difference images in the *upper* and *lower panels*, respectively, taken before and during the CME on 5 October 2012. Differences are made relative to an image five hours earlier. The dimming regions found in difference images are encircled in *cyan*.

stealthy CMEs usually do not show this level of enhancement in X-rays. Moreover, this CME was faster than 600 km s^{-1} in the LASCO field of view, even though it started slowly. In summary, this is much less stealthy than the first stealth CME in the STEREO era (Robbrecht, Patsourakos, and Vourlidas, 2009).

Nevertheless, its LCSs are elusive when we search for them in fast changes of emission features in EUV images in response to the CME. In this event, reflecting the slow development of the eruptive processes, the rate of change in coronal emission is so small that we do not detect coronal dimming or a PEA in intensity images or difference images with short temporal separations. This event will pose a serious challenge to automatic detection of coronal dimming if it relies on the rate of change in pixel intensity. In this event we observe dimming and a PEA only after the CME is observed by LASCO at the heliocentric distance of ≥ 2.5 R$_\odot$, unlike a majority of CMEs associated with a flare or filament eruption,

It is easier to observe dimming in this event from the side view as provided by STEREO. This is because the line of sight from the Earth intersects more overlying material that was not dimmed. In Figure 5 we show images in 284 Å from the *EUV Imager* (EUVI) on STEREO-B and STEREO-A in the upper and lower panels. The images in this channel

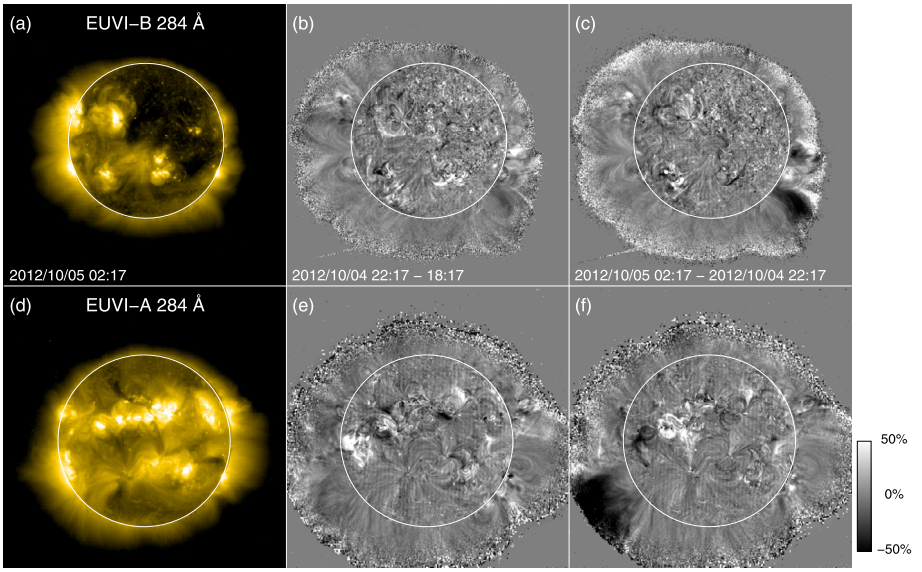

Figure 5 284 Å images from SECCHI/EUVI around the time of the CME on 5 October 2012. (**a**) – (**c**) and (**d**) – (**f**) show images from EUVI-B and EUVI-A, respectively. (**a**) and (**d**) show intensity images slightly before the CME was first detected by LASCO. (**b**) – (**c**) and (**e**) – (**f**) show percent difference images at two times, before and after the CME acceleration started in COR1 images. Images taken four hours earlier are subtracted. The *circles* represent the solar disk.

were taken only once every two hours. The leftmost panels are intensity images slightly before the CME was first detected by LASCO. The remaining panels are percent difference images from which images taken four hours earlier are subtracted. Figures 5b and e and Figures 5c and f refer to a time before and after the CME acceleration was noted in COR1 data (Figures 3c and d). Comparing Figures 5c and f, dimming in EUVI-A is more extended, consistent with the location of the source region in the western hemisphere, *i.e.* less occultation by the limb (see the inset in Figure 3a). Figures 5b and e show a trace of dimming already at 22:17 UT on 4 October. This suggests that dimming could be detected in the limb view when the flux rope moves up only slightly and takes out much lower mass than after the main CME acceleration starts. Last, dimming is weaker closer to the solar surface (see Figure 5f), suggesting that more mass at higher altitudes was evacuated by the CME.

In Figure 6 we compare the dimming regions (in Earth view) with the filament channel and the footpoints of open field lines. All the images were taken around 05:00 UT ($\pm$ 2 minutes) on 5 October. In Hα images, we may marginally trace diffuse and fragmented dark features running nearly east–west in the eastern dimming region. See Figure 6c, which shows an image from the *Solar Magnetic Activity Research Telescope* (SMART: UeNo *et al.*, 2004). This is presumably a filament channel, as it is aligned with a PIL on longitudinal magnetograms. Figure 6d shows one from the *Helioseismic and Magnetic Imager* (HMI: Scherrer *et al.*, 2012) on SDO. An extension of the filament channel to the west seems to reach the central PIL of the active region near the western dimming region. We indicate the filament channel in blue in Figures 6a, c, and d. In addition, we note in 304 Å images ribbon-like emission that separates with time on either side of the PIL. Separating flare ribbons are commonly observed in eruptive flares. Incidentally, Figure 6a shows a soft X-ray image

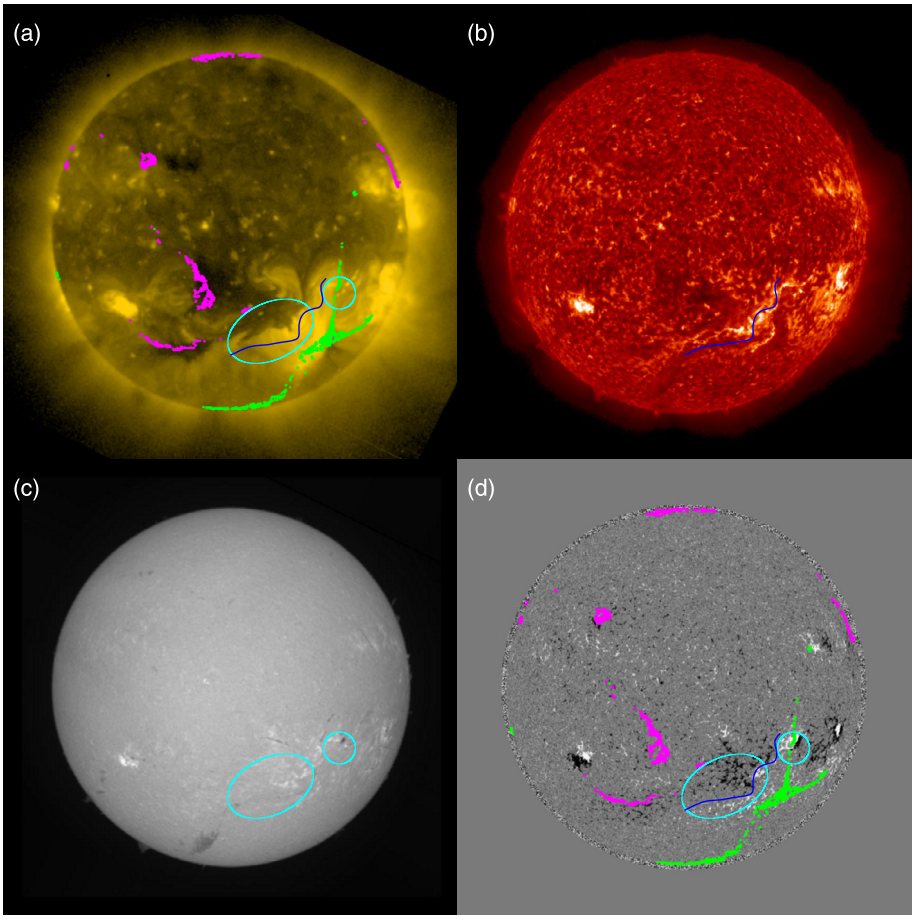

Figure 6 Relation of the dimming regions identified in Figure 4d (encircled in *cyan* in (**a**), (**c**), and (**d**)) with (1) the filament channel and PIL (*blue curve* in (**a**), (**b**), and (**d**)), and (2) the footpoints of open field lines (*pink*: negative polarity, green: positive polarity in (**a**) and (**d**)). The images shown are (**a**) GOES 15 SXI TM filter, (**b**) AIA 304 Å, (**c**) Hα (taken by the SMART at Hida Observatory), and (**d**) HMI longitudinal magnetogram. All the images were taken around 5 October 2012 05:00 UT.

from the *Soft X-ray Imager* (SXI: Lemen *et al.*, 2004) on the GOES 15 satellite, in which the PEA is more pronounced than in EUV images. This indicates that the PEA contained hot (≥ 3 MK) plasma.

To locate open field lines, we used the potential field source surface (PFSS) model as implemented in the SolarSoft by Schrijver and DeRosa (2003). About 12,000 field lines are traced from the uniform grid on the source surface (placed at the heliocentric distance of 2.5 $R_\odot$) down to the photosphere. Only their footpoints at the coronal base, ≈ 11 Mm above the photosphere, are shown in Figures 6a and 6d, color-coded depending on the polarity (green: positive, pink: negative). It is generally thought that CHs correspond to open field, but we note in this example that only part of the CHs is filled with the footpoints of open field lines. This may be because of the short and closed loops within CHs, as we note, for example, in Figures 4a and b, or because of an imperfection of the model (*cf.* Nitta and

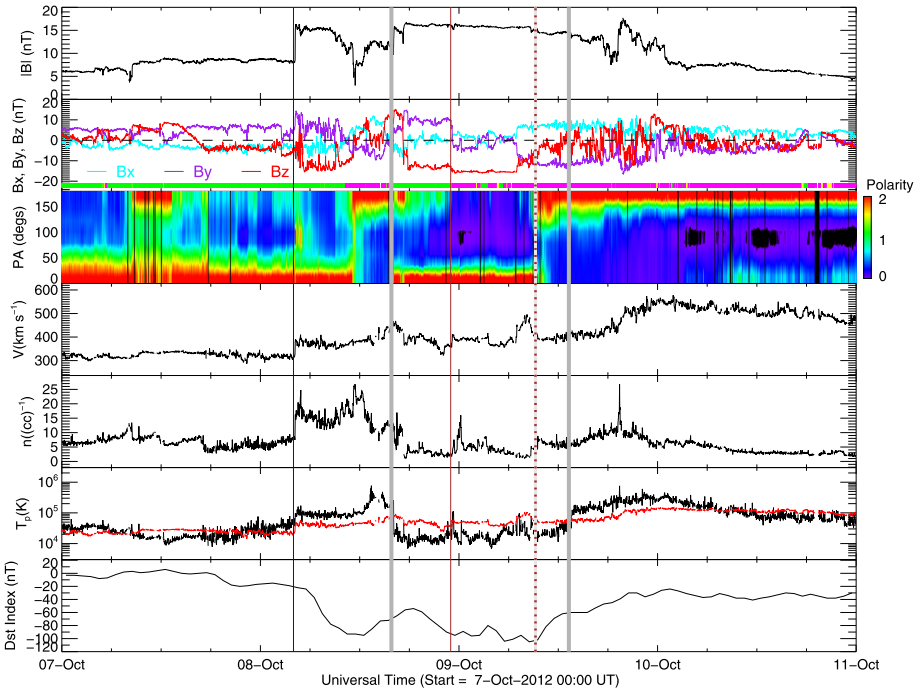

Figure 7 Solar wind data from the *Wind* satellite for an interval that includes the ICME from the CME on 5 October 2012. The plot shows from the *top panel* to the *second panel* from the *bottom* the magnetic field strength, each of the three components (in GSE coordinates) of the magnetic field, the polarity (*green*: positive/away, *pink*: negative/toward, *yellow*: uncertain), pitch angle distribution of electrons at 165 eV, proton bulk speed, density, and kinetic temperature. The *red curve* on the kinetic temperature is the expected temperature for the observed solar wind speed. The *last panel* shows the Dst index. The *blue vertical line* shows the shock. The ICME interval (from the *Wind* ICME Catalog) is indicated by *thick gray lines*. *Brown lines* show polarity reversals in the *in situ* magnetic field (*solid*) and the electron pitch angle data (*dotted*).

DeRosa, 2008). In Figures 6a and d, we find open field regions close to both the western (positive polarity) and eastern (negative polarity) dimming regions.

Now we examine how the near-Earth space environment was disturbed by the CME on 5 October 2012. Figure 7 shows time variations of the solar wind and Dst index during 7 – 11 October 2012. The solar wind magnetic field and plasma data come from the *Wind* satellite, obtained from https://spdf.gsfc.nasa.gov/pub/data/wind/. The top two panels show the magnetic field amplitude and three components in goecentric solar ecliptic (GSE) coordinates. In addition, the polarity is shown color-coded in the bottom part of the second panel (green: positive, pink: negative). The polarity sector is determined from the magnetic field vector (B_x, B_y) if it is aligned within $\pm 75°$ from the nominal Parker angle calculated from the observed solar wind speed. No polarity is assigned (yellow) if the magnetic field vector is more than $\pm 75°$ away from the Parker angle. The third panel shows the pitch angle distribution of suprathermal (≈ 165 eV) electrons from the *3-Dimensional Plasma and Energetic Particle Investigation* (3DP) instrument. The fourth to sixth panels show the bulk speed, density, and kinetic temperature of solar wind protons. The last panel shows the Dst index.

The first sign of the disturbances is the shock around 04:00 UT on 8 October. It is followed by a sheath region and then by an ICME, starting around 15:00 UT. The ICME shows smooth field rotation, which is suitable for flux rope fitting. Marubashi, Cho, and

Ishibashi (2017) used a torus fitting and found that the magnetic cloud has right-handed helicity, which often comes from an eruption in the southern hemisphere (Marubashi, 1997; Bothmer and Schwenn, 1998). The decrease in Dst index occurred in two steps that correspond to the sheath region and ICME. In the second part, the minimum Dst index reached −105 nT. The geomagnetic storm in the NOAA scale was G2 (Kp = 6+). A strong and rapid electron acceleration event occurred in the radiation belt during the geomagnetic storm and was observed by the *van Allen Probes* (Reeves *et al.*, 2013; Thorne *et al.*, 2013; Kurita *et al.*, 2016).

The polarity of the magnetic field turned from positive to negative during the ICME. The ICME was followed by an HSS with negative polarity, presumably coming from the CH next to the eastern dimming region (see Figure 6a). There is also an indication of a mismatch of the sector boundary crossing time as sensed by the change in pitch angle of suprathermal electrons (that began around 09:15 UT on 9 October) with that in direct magnetic field measurement (around 23:00 UT on 8 October). These times are indicated by the two kinds of vertical lines in brown. This phenomenon may be indicative of interchange reconnection of expanding active region loops with open field lines near a sector boundary, as suggested by Crooker *et al.* (2004). Figures 6a and d may indeed indicate such a mechanism because of the location of the dimming regions relative to the CHs or open field regions. However, the *in situ* magnetic field is predominately southward during this time, so the azimuthal angle of the field is poorly defined. Thus the sector boundary crossing as determined from the magnetic field remains somewhat ambiguous.

4. Other Stealthy Events with Significant Heliospheric Impact

In this section, we give examples of more challenging events in which the LCSs of the CME are more elusive than the October 2012 event. In searching for stealthy CMEs, our primary interest is in events that impact the heliosphere in a significant manner (*e.g.* Nieves-Chinchilla *et al.*, 2013; Kilpua *et al.*, 2014). Assuming a usual power-law distribution of the frequency of CMEs or solar eruptions with their magnitude (defined, for example, by kinetic energy), there should be many more weaker events, but it is questionable that such events in general give rise to large-scale and observable heliospheric disturbances, unless the ICME is unambiguously traced back to one of those at the Sun. Therefore we instead started with the ICME catalogs mentioned in Section 3 and searched for those events where a CME is found that seems to explain the ICME but its origin is not readily identified. We made movies of STEREO/SECCHI data, when available, for each event. This was to establish a solid link between ICMEs and CMEs, making use of the overlapping height or elongation covered by EUVI, COR, and the *Heliospheric Imager* (HI).

The selected events are summarized in Tables 1 and 2, which list the solar and 1 AU manifestations, respectively. We used the common event identification (ID) to link the two observational domains. These events are by no means meant to make up a comprehensive list of stealthy events, nor are they selected using rigorous criteria. In event 9, the CME–ICME connection is less well established than the other events because the *in situ* signatures are dominated by a CIR,[7] but Marubashi, Cho, and Ishibashi (2017) isolated flux rope signatures embedded in solar wind data (Webb and Nitta, 2017). In event 13, there was no STEREO data, which makes it harder to determine with confidence the front side origin of the CME

[7] See http://solar.gmu.edu/heliophysics/index.php/05/31/2013_15:30:00_UTC and Webb and Nitta (2017).

Table 1 Partial list of stealthy events (solar)

1 ID	2 Detection time	3 Speed (height range)	4 CPA	5 AW	6 Loc.	7 CH	8 LCS	9 CL
1	2010/06/16 14:54	236 (2.7 – 22.5)	61	153	S25 E06	Y	P, D	1
2	2010/12/23 05:00	286 (2.6 – 20.9)	241	126	S55 W20	Y	P, D	1
3	2011/01/19 10:54*	74 (2.4 – 5.4)	306	≥ 103	S35 W05	N	P, D	3
4	2011/01/30 12:36	120 (2.7 – 10.3)	184	264	S25 E40	N	P, D	2
5	2011/03/03 06:12	263 (2.5 – 14.9)	169	206	S20 W10	N	P, D	2
6	2011/03/25 14:36	119 (2.6 – 7.8)	205	≥ 191	S15 E30	Y	P, D	2
7	2011/05/25 13:26	561 (3.0 – 14.7)	321	78	S18 W25	Y	P, D	2
8	2012/10/05 02:48	612 (2.5 – 24.6)	258	284	S25 W15	Y	P, D	1
9	2013/05/27 00:24	224 (3.1 – 22.9)	15	94	N10 E30	Y	D	3
10	2013/06/02 20:00	222 (2.4 – 7.2)	93	87	N10 W18	Y	P, D	1
11	2013/06/23 22:36	174 (2.6 – 8.0)	284	174	N25 W05	Y	P, D	1
12	2013/06/30 03:12	289 (2.8 – 7.2)	304	132	S10 W15	Y	P, D	2
13	2015/01/03 03:12	163 (3.1 – 15.1)	118	153	S25 E06	Y	P, D	3
14	2016/10/08 23:24*	182 (2.7 – 16.5)	26	255	S05 E17	Y	D	3

1: Event ID. 2: Time of the first CME detection by LASCO/C2, hours are given in UT (*: not from the Coordinated Data Analysis Workshop (CDAW) LASCO CME catalog). 3: CME linear speed in $\mathrm{km\,s^{-1}}$ by LASCO (over the height range in $R_\odot$). 4: CME central position angle in degrees in LASCO data. 5: CME angular width in degrees measured in LASCO images. 6: Location of the CME source region in heliographic coordinates. 7: Proximity of the CME source region to a CH (Yes or No) on the basis of visual inspection of images. 8: Observed low coronal signatures (LCSs) of the CME (P: post-eruption arcade, D: dimming). 9: Confidence level (1: highest – 3: lowest).

and the time range in which the CME formed and underwent significant acceleration. This event is discussed in Section 4.4 together with other examples in Sections 4.1 – 4.5.

In Table 1 the basic information of the CMEs is given in columns 2 – 5, namely, the time of first detection by LASCO C2, the linear speed, the central position angle (measured counterclockwise from solar north), and the angular width. They have been taken from the CDAW LASCO CME catalog at https://cdaw.gsfc.nasa.gov/CME_list/, except for events 3 and 14, where we measured the CME parameters. Event 3 is not included in the catalog. As of writing this article, the catalog is not updated to the time of event 14. In column 3, we add the range of heliocentric distance (height) in $R_\odot$ that is used to derive the CME speed. Some of the CMEs are so diffuse that they cannot be traced beyond 10 $R_\odot$. Column 8 shows the LCSs that we associate with the CME. We specifically searched for a PEA and coronal dimming, and both were found in most events. The location of the source region in column 5 refers to the PEA or dimming region. When there are more than one dimming region, we list their average location. The location should be understood as having a range of $\pm 10^\circ$ from the coordinates in column 5, reflecting both the intrinsic size of the source and the uncertainties of locating it. Column 7 indicates if there is a CH close to the source region, typically within 10° in heliographic coordinates. In addition to dark regions not overlapping with filaments in AIA coronal images, we also include the regions where open field lines are rooted, as calculated with the PFSS model (see Figure 6). Last, we assign the confidence level (1, 2, or 3) for the identification of the source region. For events with confidence level 1, the source region has probably been correctly identified. For events with confidence level 2, the identified source region might be only part of more than one region that became the

Table 2 Partial list of stealthy events (1 AU)

1	2	3	4	5	6	7	8	9	10	11
ID	Dist. start time	Dur.	v_{max}	Shock	B_{max}	FR	Pol.	HSS	Dst	Kp
1	2010/06/20 20	1.8	410	N	7.7	WNE, R	+	N	−11	2+
2	2010/12/28 03	0.5	360	N	14.0	NES, R?	+	N	−43	4o
3	2011/01/24 07	1.2	400	N	8.2	NES, R	+	N	−14	3o
4	2011/02/04 13	0.3	470	N	23.3	NES, R?	−	Y	−63	6−
5	2011/03/06 03	2.1	530	N	7.3	–	−	N	−27	4−
6	2011/03/29 16	1.5	390	N	14.6	–	+	N	−4	3+
7	2011/05/28 01	0.8	540	N	13.3	SWN, R	−	Y	−80	6+
8	2012/10/08 04	1.5	420	Y	16.7	ESW, R	+−	Y	−105P	6+
9	2013/05/31 15	1.5	410	Y	24.5	–	−+	Y	−119P	7o
10	2013/06/06 03	1.9	510	N	13.5	WSE, L	+	N	−73P	6−
11	2013/06/27 14	2.0	450	Y	13.6	WSE, L	−+	Y	−98P	6+
12	2013/07/05 01	2.6	370	N	13.0	ESW, R	+	N	−77P	5−
13	2015/01/07 06	0.5	470	N	22.6	SEN, L	−+	N	−99Q	6+
14	2016/10/12 21	1.6	370	Y	24.8	SEN, L	−	Y	−104Q	6+

1: Event ID. 2: The disturbance start time in the closest hour (in UT), taken from the *Wind* or Richardson and Cane Catalog. The only exception is event 7, where the observed shock arrival time is entered. 3: Duration in days of the event from the start time in column 2 to the ICME end time. 4: Observed maximum solar wind speed in $km\,s^{-1}$. 5: If a shock is observed (Yes or No). 6: Observed maximum magnetic field strength in nT. 7: Flux rope type, if observed. 8: IMF polarity from a day before the start time (in column 2) to a day after the end of the ICME. 9: If the ICME is followed by a solar wind HSS within 12 hours (Yes or No). 10: Minimum Dst index (nT), taken from the official Dst index page at the World Data Center for Geomagnetism, Kyoto (http://wdc.kugi.kyoto-u.ac.jp/dstdir/). P stands for "Preliminary" and Q "Quicklook". 11: Maximum Kp index, as found in the official Kp index page at the German Research Centre for Geosciences (GFZ) (http://www.gfz-potsdam.de/en/section/earths-magnetic-field/data-products-services/kp-index/).

CME. For events with confidence level 3, we have found a best candidate of the source region, but do not claim that it is correct, calling for further investigation.

Table 2 gives information on the 1 AU signatures of the stealthy CMEs. In column 2, the start time of the disturbance is shown. This is taken from one of the four ICME catalogs mentioned in Section 3, with the exception of event 9. As noted earlier, this event was dominated by a CIR, and accordingly, it was not included in any of the above ICME catalogs. For this event, we show the shock arrival time at the *Wind* satellite. Columns 3 – 6 give the duration of the ICME, the maximum solar wind speed, the existence of a shock, and the maximum magnetic field strength. Column 7 shows a simple estimate of the type of the flux rope (Bothmer and Schwenn, 1998; Mulligan, Russell, and Luhmann, 1998) on the basis of the rotation of the field in the Y–Z plane. The associated handedness of helicity is also given. Column 8 shows the polarity of the magnetic field during the ICME period. Double signs indicate that the ICME coincides with the passage of a sector boundary. Column 9 shows whether the ICME is followed by a solar wind HSS within 12 hours. The last two columns show the magnitudes of geomagnetic disturbances in terms of the Dst and Kp indices.

4.1. CME on 16 June 2010

This event occurred in an early phase of Solar Cycle 24. Figure 8 shows white-light and EUV images of this event. In COR2 data (Figures 8a and c) there is evidence for a flux

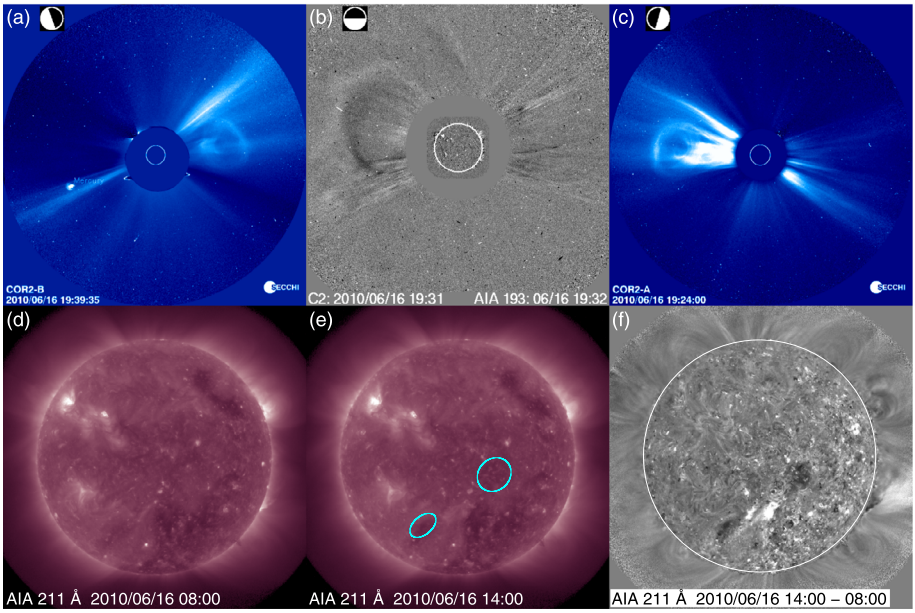

Figure 8 CME on 16 June 2010. (**a**) COR2-B, (**b**) LASCO C2, and (**c**) COR2-A images. The LASCO image is a difference image. The *small symbols* next to the *labels* indicate the visible side of the Sun from a viewpoint above the north pole for each of the platforms. (**d**) and (**e**): AIA 211 Å images during the CME acceleration phase (from the COR1 observations) separated by six hours. (**f**): Difference of images in (**d**) and (**e**) with the differential solar rotation corrected for. Two dimming regions found in (**f**) are encircled in *cyan* in (**e**).

rope within the CME, but the CME was so diffuse in Earth view that we need difference images to see it (Figure 8b). This CME was presented by Vourlidas *et al.* (2011) as showing remarkable rotation. They also acknowledged the stealthiness of the event and located the CME source region by projecting a prominence in EUVI 304 Å images onto a marginal filament in AIA 171 Å images. Here we searched for a PEA and dimming around the time of the CME formation and acceleration as seen in COR1 images (*i.e.* 08:00 – 14:00 UT on 16 June). Figure 8f shows a difference of two AIA 211 Å images taken six hours apart, as shown in Figures 8d and e. We note two bright patches with dimming regions on either side aligned northwest–southeast. The bright patches probably represent part of a PEA, which is located slightly south of the filament (channel) as found by Vourlidas *et al.* (2011); see their Figure 1. The solar wind disturbances from this CME started on 21 June 2010. They are minor, but are included in the ICME catalogs referenced earlier.

4.2. CME on 3 March 2011

This CME again clearly contained a flux rope as seen by COR2 (Figures 9a and c). In LASCO data, it emerged from the south (Figure 9b). There was only one small active region (AR 11165) in the southern hemisphere, located at S22 W09 as of 00:00 UT on 3 March 2011. Pevtsov, Panasenco, and Martin (2012) applied a geometric triangulation method to STEREO-A and B data, and estimated the CME source region to be south of the AR, at $S35° \pm 10°$, $W15° \pm 10°$. This was aligned with an empty filament channel. Using difference images with long temporal separations around the initial acceleration of the CME in COR1

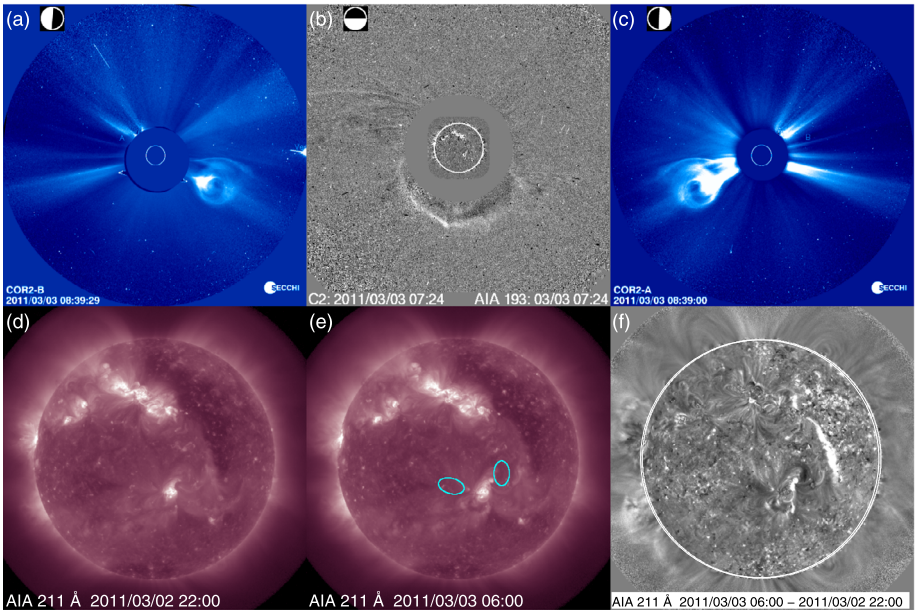

Figure 9 CME on 3 March 2011. (**a**) COR2-B, (**b**) LASCO C2, and (**c**) COR2-A images. The LASCO image is a difference image. The *small symbols* next to the *labels* indicate the visible side of the Sun from a viewpoint above the north pole for each of the platforms. (**d**) and (**e**): AIA 211 Å images during the CME acceleration phase (from the COR1 observations) separated by six hours. (**f**): Difference of images in (**d**) and (**e**) with the differential solar rotation corrected for. Two dimming regions found in (**f**) are encircled in *cyan* in (**e**).

images, we find dimming regions and a PEA around S20 W10 (see Figures 9d – e). The corresponding dimming is also centered around S20 as captured in EUVI difference images. Figure 9f also shows a narrow brightening to the west across the equator. This was located at the boundary of a coronal hole in the northwestern quadrant. This brightening preceded the CME in question, and may have been correlated with a diffuse outflow seen only in COR1 data.

The *in situ* manifestations of this CME are not clear. Solar wind data during 6 – 9 March do not show a particularly strong or organized magnetic field, but there was a period in which the solar wind smoothly decreased and the proton temperature was consistently lower than what was expected from the observed solar wind speed. Only the Richardson and Cane catalog includes the period as an ICME, but with the lowest quality factor. It is possible that the CME on 3 March was deflected south by the coronal hole in the northern hemisphere, and that the *in situ* data were also contributed by other CMEs before and after the CME shown in Figure 9.

4.3. CME on 23 June 2013

This CME could have easily been overlooked if there had been no ICME or geomagnetic storm (Dst of almost −100 nT) during 27 – 29 June 2013. Figure 10 shows coronagraph and EUV images. There was a slow filament eruption in the northeastern quadrant, close to the central meridian, late on 22 June, producing a slow and long-lasting CME. About a day later, a diffuse and slow CME was seen from the west in LASCO data (Figure 10b).

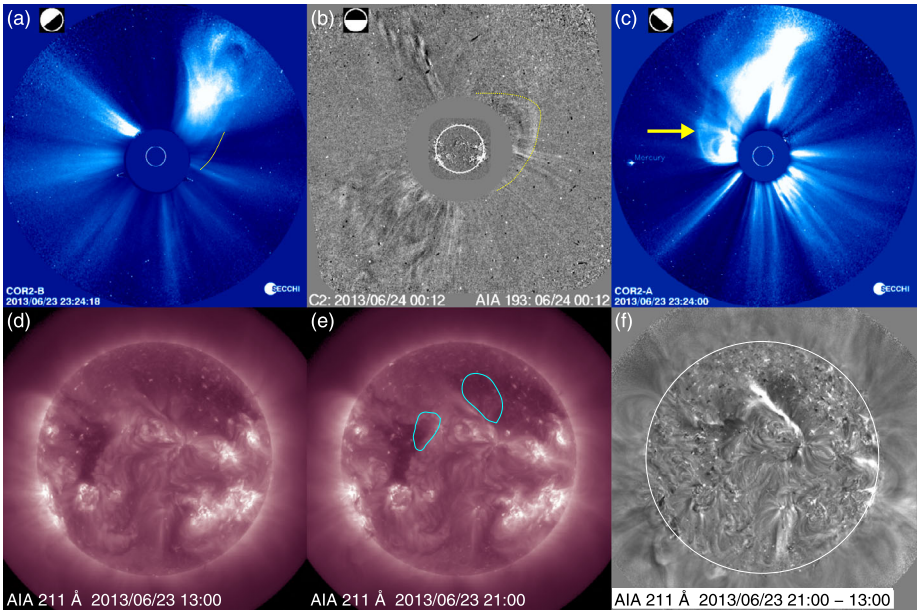

Figure 10 CME on 23 June 2013. (**a**) COR2-B, (**b**) LASCO C2, and (**c**) COR2-A images. The LASCO image is a difference image. The *small symbols* next to the *labels* indicate the visible side of the Sun from a viewpoint above the north pole for each of the platforms. (**d**) and (**e**): AIA 211 Å images during the CME acceleration phase (from the COR1 observations) separated by six hours. (**f**): Difference of images in (**d**) and (**e**) with the differential solar rotation corrected for. Two dimming regions found in (**f**) are encircled in *cyan* in (**e**). The CME in question is indicated in *yellow* in (**a**) – (**c**).

Even around this time, the slow CME from the earlier filament eruption dominated COR2 (both STEREO-A and B) images (see Figures 10a and c), and it was hard to recognize the diffuse CME (indicated in yellow) that was probably launched close to the central meridian. Note that STEREO was already 140° to the east and west of the Sun–Earth line, and it was difficult to observe Earth-directed CMEs.

AIA images show that there was an eruption around N10 W05 at 03:00 UT on 23 June. However, this likely did not escape the Sun. Instead, difference images with long temporal separations indicate another slow eruption to the north after 15:00 UT. See the double dimming regions and a PEA between them in Figure 10f. Even though STEREO data give us an impression that the CME from the earlier filament eruption had an extension to south, this was an independent CME (Figures 10a and c). In *in situ* data (not shown), the ICME clearly contained the WSE-type flux rope, followed by a high-speed solar wind stream. Next to the eastern dimming region was a coronal hole (Figure 10e), which was presumably responsible for the HSS that followed the ICME. This coronal hole was the return of the hole that was attributed to event 9 one rotation before (Webb and Nitta, 2017). There are certain similarities between these two events, such as a preceding slow filament eruption to the north, but the on-disk LCSs in this event are much more clearly identified than in event 9.

4.4. CME on 3 January 2015

This CME started much more stealthily than the four events discussed so far. White-light and EUV images are shown in Figure 11. There were at least two bright streamers sticking

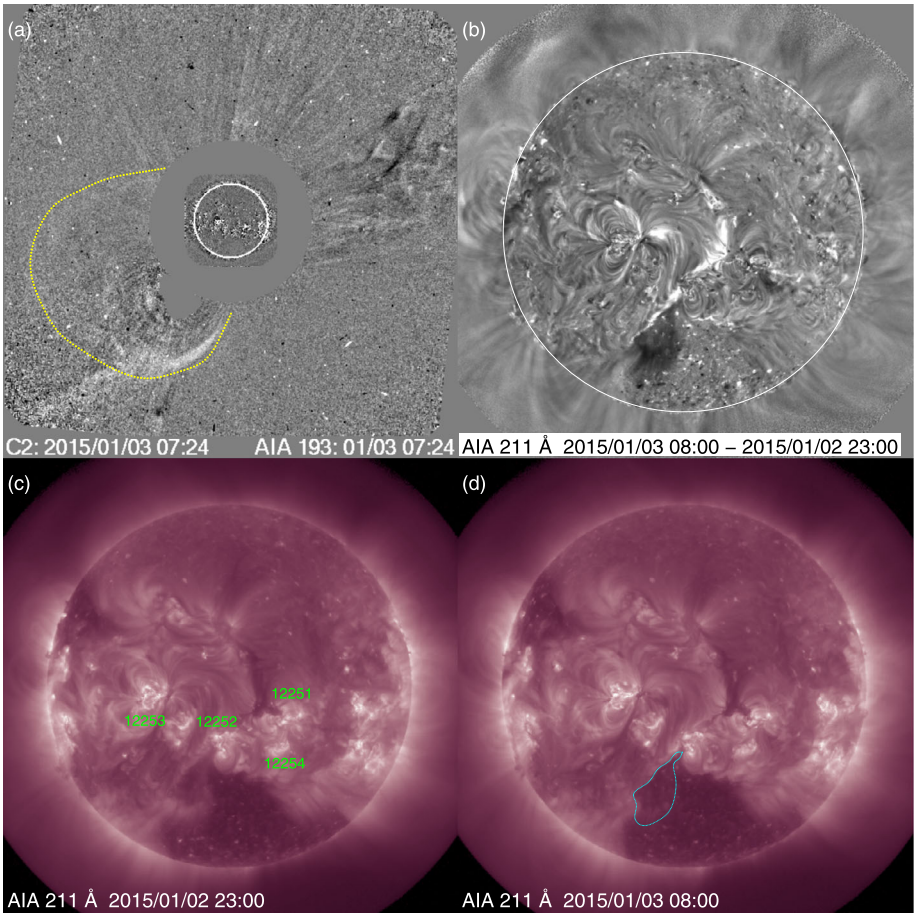

Figure 11 Slow and diffuse CME on 3 January 2015. (**a**) LASCO C2 image. The CME front is indicated by a *yellow curve*. (**c**) and (**d**) show AIA 211 Å images taken 9 hours apart. (**b**) The difference of the images in (**c**) and (**d**), corrected for differential rotation. The dimming region found in (**b**) is marked in *cyan* in (**d**). Active regions are indicated in (**c**).

out around position angle of 150°, saturating the processed LASCO image in Figure 11a as a flat gray area. Only the northernmost streamer seemed to be involved in this CME. On the other hand, the CME was much wider than the azimuthal expanse of the streamers, suggesting that this was not a classic streamer blowout CME. It started very slowly with a diffuse front, as encircled in yellow in Figure 11a. A second-order polynomial fit to the height-time relation yields an acceleration of 3.65 $\mathrm{m\,s^{-2}}$, but the linear speed within the LASCO field view was still only 163 $\mathrm{km\,s^{-1}}$. STEREO was nearly opposite to Earth and no data were downlinked, so it is in principle possible that this CME came from the backside.

However, difference images in the AIA 211 Å channel with long temporal separations show a clear dimming that overlaps the northeastern part of the extended CH that contains the south pole (see Figures 11b – d). This can be seen even in intensity images, giving an impression that the CH widened. A narrow brightening is seen to the immediate northeast of

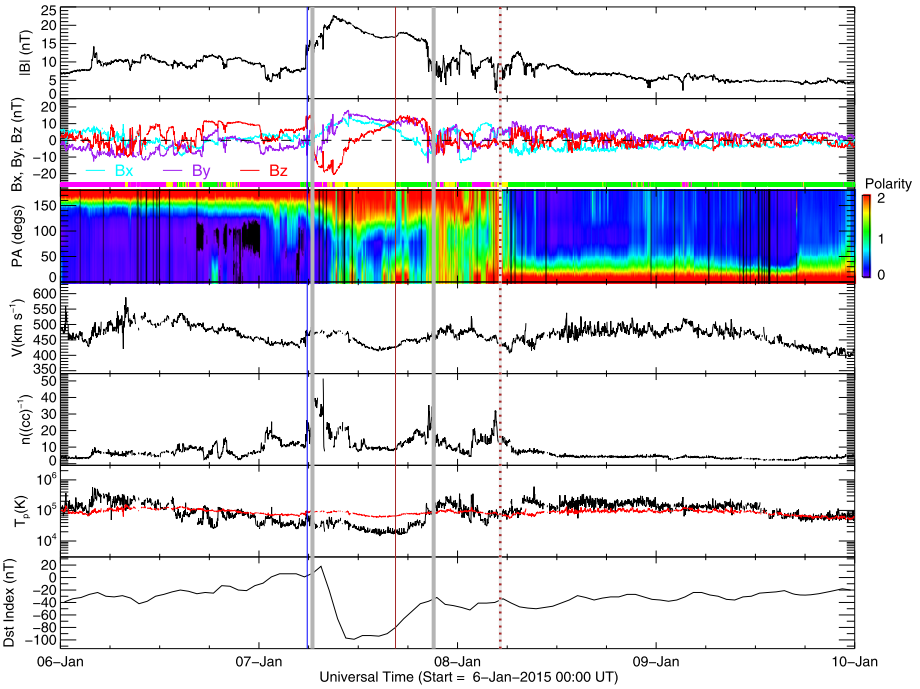

Figure 12 Solar wind data from the *Wind* satellite for the interval of 6 – 10 January 2015. The plot shows from the *top panel* to the *second panel* from the *bottom* the magnetic field strength, each of the three components (in GSE coordinates) of the magnetic field, the polarity (*green*: positive/away, *pink*: negative/toward, *yellow*: uncertain), pitch angle distribution of electrons at 165 eV, proton bulk speed, density, and the kinetic temperature. The *red curve* on the kinetic temperature is the expected temperature for the observed solar wind speed. The *last panel* shows the Dst index. The *blue vertical line* shows the intensification of the magnetic field that marks the onset of the geomagnetic storm. The ICME interval (from the *Wind* ICME Catalogue) is indicated by *thick gray lines*. *Brown lines* show polarity reversals in the *in situ* magnetic field (*solid*) and the electron pitch angle data (*dotted*).

the dimming region. Although in Figure 11b it appears to be connected to the western side of AR 12253 (see Figure 11c), which produced several non-eruptive flares, the brightening may represent something similar to a PEA, suggesting the possibility that an area beyond AR 12253 may have been involved in the eruption. However, we cannot proceed at present with this line of thought because there are no STEREO data.

This CME is the only candidate to be responsible for the 1 AU disturbances that started on 7 January. Figure 12 gives a solar wind and Dst plot in the same format as Figure 7. First, the period contains a relatively short geomagnetic storm peaking at Dst = −99 nT. The Kp index peaked at 6+ (plotted as Kp = 7 in the quick-look plots by NOAA Space Weather Prediction Center (SWPC) and thus classified as a G3 storm). Within the short period of the ICME, the magnetic field rotation was consistent with right-handed helicity, which contradicts the expectation for an eruption from the southern hemisphere. Unlike the October 2012 event, the pitch angle distribution shows much more bidirectional streaming within the ICME proper. Although there is a short pitch angle reversal nearly coincident with the magnetic polarity reversal marked by the brown vertical line near 16:30 UT on 7 January, more analysis is needed to determine whether there is a mismatch in time between the sector boundary crossing indicated by the suprathermal electrons and that indicated by

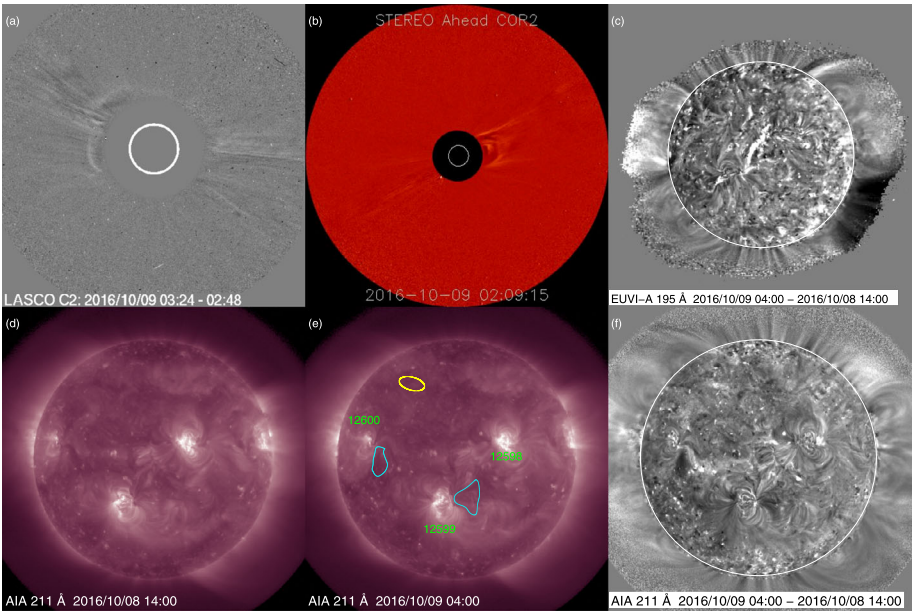

Figure 13 Slow and diffuse CME on 8 – 9 October 2016. (**a**) LASCO C2 image. (**b**) COR2-A image. (**c**) EUVI-A (195 Å) difference image. (**d** – **e**) Two 211 Å images taken 14 hours apart. (**f**) The difference of the images in (**d**) and (**e**). The difference images are corrected for differential rotation. In (**e**) the dimming regions and the location of the minor filament eruption are marked in *cyan* and *yellow*, respectively.

the magnetic polarity reversal. After the ICME, it is clear that there has been a crossing of the sector boundary as the pitch angle of the electrons shows a change to a unidirectional sunward flow (beginning around 5:10 UT on 8 January, indicated by the dotted brown line).

We note that according to the PFSS model, the polarity of the extended CH in the southern hemisphere was negative, which accounts for the *in situ* data before the ICME. However, it is not clear where the subsequent positive-polarity sector came from. The model shows positive polarity in the CH around E60, but we need it far to the west, such as the western periphery of AR 12253, to be consistent with the timing. Therefore we find it difficult to interpret the data in terms of magnetic field extrapolation. Another puzzling fact is that the extended CH was dominated by strong negative polarity only up to S60, as revealed in HMI magnetograms. At higher latitudes, the field could have been weaker or less unipolar. The footpoints of open field lines as calculated using the PFSS model are not detected in the coronal hole poleward of S60. This may have to do with the incomplete magnetic field reversal at the south pole during the time of interest. While such a solar cycle effect needs to be investigated more closely, it is presumably important to take this unique phase of a solar cycle into account in order to better understand this event.

4.5. CME on 8 – 9 October 2016

A diffuse CME was first seen in the northeastern sector (Figure 13a), and then it surrounded the whole occulting disk (*i.e.* a full halo CME) by 06:00 UT on 9 October. It was seen on the western side of COR2-A (Figure 13b). STEREO-A was 148° east of the Sun–Earth line. Without a third view, such as from STEREO-B, the CME longitude could have been

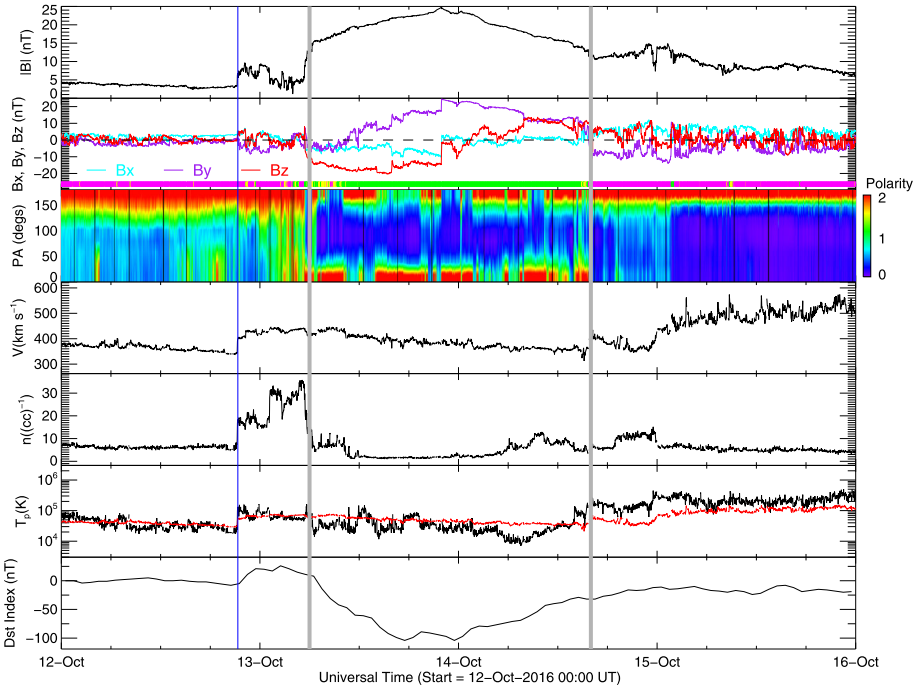

Figure 14 Variations in solar wind and Dst index for the interval of 12 – 16 October 2016. The plot shows from the *top panel* to the *second panel* from the *bottom* the magnetic field strength, each of the three components (in GSE coordinates) of the magnetic field, the polarity (*green*: positive/away, *pink*: negative/toward, *yellow*: uncertain), pitch angle distribution of electrons at 165 eV, proton bulk speed, density, and kinetic temperature. The *red curve* on the kinetic temperature is the expected temperature for the observed solar wind speed. The *last panel* shows the Dst index. The *blue vertical line* shows the shock. The ICME interval (from the Richardson and Cane Catalog) is indicated by *thick gray lines*.

anywhere between E148 and E00. However, there were no compelling eruptive signatures in EUVI-A images that extended to E58, therefore we conclude that the CME was from the front side and Earth-directed. Moreover, this was the only halo CME that could account for the G2 geomagnetic storm (Dst < -100 nT) that started late on 12 October as shown in Figure 14.

It is very challenging to find the source region of this CME. The CME, while still unclear, appears to have passed the COR1-A field of view roughly between 18:00 UT on 8 October and 02:00 UT on 9 October. We searched for possible signatures of the CME in AIA data over a longer interval. Two AIA 211 Å images, 14 hours apart, are shown in Figures 13d and e. There was a minor filament eruption in the northern hemisphere during 15:00 – 16:00 UT on 8 October (indicated in yellow in Figure 13e), but it seems to be too localized to account for the extended CME, even though it may have helped destabilize other regions, causing them to erupt. We instead tried to find dimming in difference images with long temporal separations. Figure 13f is an example, which shows dimming on the western side of AR 12599 and southwest of AR 12600. We are aware of caveats of difference images with long temporal separations, such as the tendency of the western (eastern) hemisphere to become brighter (darker) as a result of the solar rotation combined with the variation of the area *per* pixel with the distance from the disk center. However, these dimming regions ap-

pear consistently for different sets of the times used for the difference images and should be real. More importantly, EUVI-A images also show extended dimming over the southwest limb (Figure 13c), leading us to envision the dimming in the southern hemisphere as a key element of the CME. We tentatively use the center of the two dimming regions in AIA images as the location of the CME source region.

The 1 AU disturbances from this CME are shown in Figure 14. The *in situ* signatures are characterized by a shock late on 12 October, followed by a sheath region and a magnetic cloud that lasted for 34 hours. The magnetic field vector shows smooth rotation for 1.5 days. It is noteworthy that such a clear coherent structure resulted from a CME whose LCSs did not seem to be contained in one AR or filament channel. The *in situ* flux rope was again right-handed, not following the expectation for an eruption from the southern hemisphere. The magnetic polarity at 1 AU alternates within the magnetic cloud, while the electron pitch angle distribution is indicative of bidirectional streaming, typical of many ICMEs. However, there is no clear indicator of a sector boundary crossing. The high-speed stream following the ICME probably arises from the small coronal hole that overlaps with the eastern dimming regions. In fact, this region provides open field lines in the ecliptic for more than two days, according to the PFSS model.

5. Discussion

Earth-affecting CMEs are sometimes stealthily launched without clear LCSs. These events constituted about 12% of the intense (Dst ≤ -100 nT) geomagnetic storms in Solar Cycle 23 (Zhang *et al.*, 2007). The frequency of similar events could have been higher during the recent extended solar minimum (see Ma *et al.*, 2010; Kilpua *et al.*, 2014) if we lowered the threshold for the magnitude of storms, taking into account the solar minimum conditions. In the present article we investigated similar phenomena that were observed during Solar Cycle 24. In this first study, we did not select events with rigorous criteria for the absence of LCSs, the magnitude of geomagnetic storms, or other 1 AU properties. However, it is interesting to note in Table 2 the three Dst ≤ -100 nT events. Three events are a significant fraction of 17 such events in Solar Cycle 24.

There seem to be different levels of difficulty of finding LCSs. In this article we first examined the 5 October 2012 CME as a relatively easy case for finding LCSs. This CME was initially labeled a stealth CME by the VarSITI/ISEST program, although it was not included in the study by D'Huys *et al.* (2014), who selected the events using rigorous criteria. Even though the CME started off very slowly, its linear speed in the LASCO field of view was over 600 km s^{-1} and it was associated with a long-duration B-class flare. The slow development of the CME close to the Sun indicates that the eruption started well before the CME was first observed by LASCO. Data from STEREO, COR1 in particular, revealed that the CME formation and initial acceleration lasted only a few hours, however, and not as long as 20 hours, before the first detection by LASCO. We find the low coronal response to the eruption to be more pronounced during and following the initial acceleration. AIA images, especially in 211 Å, 193 Å, and 335 Å channels, reveal the PEA and dimming regions as the LCSs of the CME when we make difference images with long temporal separations that encompass the CME formation and acceleration. The PEA and dimming regions may not be isolated in intensity images or running-difference images that are good at capturing an elevated rate of changes. Without knowing the time range of CME formation and acceleration, one could be easily misled to other regions that show some changes at earlier times (Figure 2). These regions may have contributed to destabilizing the region that actually erupted, but the latter

should be isolated as the CME source region. It is important to find the region that actually erupted when correlating the magnetic field properties of ICMEs with solar eruptions (*e.g.* Marubashi, Cho, and Ishibashi, 2017).

We also studied other Earth-affecting CMEs whose LCSs were more elusive. They are typically slow CMEs (Robbrecht, Patsourakos, and Vourlidas, 2009; Ma *et al.*, 2010; D'Huys *et al.*, 2014; Kilpua *et al.*, 2014). In a number of events, we can find PEAs and dimming regions, and locate the source regions (Sections 4.1 – 4.3.), using the above technique of finding the time range of CME formation and acceleration in STEREO COR data and making AIA difference images with long temporal separations. However, we acknowledge that the LCSs are not as convincingly identified in AIA data in several events, including those in Sections 4.4 – 4.5. This is partly due to the absence of STEREO observations in favorable angular separation (*e.g.* 50° – 130°) from the Sun–Earth line. Even with STEREO data, however, it would still be challenging to find the LCSs in some events because the CME is seen to be clearer only beyond a few solar radii, from where it is hard to trace the CME back to the low corona. This is similar to the prototype stealth CME studied by Robbrecht, Patsourakos, and Vourlidas (2009).

Does the detection of the LCSs depend simply on the magnitude or energy of the CME in competition with the sensitivity of current instrumentation, as proposed by Howard and Harrison (2013), or does it reflect other factors, not only the CME initiation height (*e.g.* Robbrecht, Patsourakos, and Vourlidas, 2009) but also different mechanisms and processes for the eruption? We might hypothesize that some stealthy events are triggered more significantly by ideal processes such as torus instability. Phenomenologically, eruptions from such processes may resemble expanding loops that smoothly accelerate to become a CME. Another hypothesis that is inspired by the October 2016 event is that stealthy eruptions may involve larger areas than single active regions and filament channels. These events may make it hard to reconcile the chirality of the flux rope at 1 AU with the hemisphere from which the CME originates.

Although it is not necessary to generalize all the stealthy events in one category, one common property appears to be that none of them have recurred as homologous events. They presumably represent once-in-life processes of energy build-up in and around active regions, as suggested in numerical simulations of stealth CMEs (*e.g.* Lynch *et al.*, 2016). Furthermore, the LCSs for stealthy CMEs tend to be found close to CHs and open field regions, as found earlier by D'Huys *et al.* (2014) for rigorously defined stealth CMEs. The HSSs from these regions and the associated CIRs may strongly affect the propagation of slow CMEs (Liu *et al.*, 2016). They not only deflect CMEs, but also accelerate and compress them. It is possible that the structure that results from interaction of an HSS with weak CMEs can become more geoeffective than if they arrive separately at 1 AU. We note that the largest geomagnetic storms in our sample of events involved an ICME followed by an HSS (Table 2). Moreover, this effect could be more extensive than indicated directly by *in situ* data, which are currently limited close to the ecliptic plane. When the ICME overlaps with a sector boundary, we may note a mismatch of the times when the polarity changes, as sensed by suprathermal electrons and measured *in situ*. Crooker *et al.* (2004) discussed this phenomenon in terms of interchange reconnection between expanding loops from ARs and open field lines. Interchange reconnection may also play a major role in driving stealthy eruptions in the corona. For a better understanding of the origin of stealthy CMEs, we emphasize the importance of numerical work of solar eruptions that also incorporate interchange reconnection (*e.g.* Lugaz *et al.*, 2011; Masson, Antiochos, and DeVore, 2013; Lynch *et al.*, 2016).

Last, in this work we did not conduct a quantitative analysis of AIA images. The origin of stealthy CMEs might be better understood with thermodynamic parameters, as obtained with differential emission measure analysis of AIA data (*e.g.* Cheung *et al.*, 2015).

6. Summary

We have shown that we need to compare AIA images taken in large temporal separations to find weak LCSs, coronal dimming, and a PEA in particular, in stealthy eruptions or slow CMEs. STEREO COR data provide the time range to examine AIA data that matches CME formation and acceleration. Even with AIA data with broad temperature coverage, challenging events do exist, for which the LCSs are not convincingly identified. A key to understanding some of the stealthy events may be their proximity to CHs, which will have consequences in the way the eruption is driven and how it eventually disturbs the heliosphere.

Acknowledgements We thank the referee for detailed comments that greatly helped us improve the article. This work was motivated by scientific discussions through the International Study of Earth-affecting Solar Transient (ISEST), one of the four elements of the Variability of the Sun and Its Terrestrial Impact (VarSITI) program under the Scientific Committee on Solar Terrestrial Physics (SCOSTEP). The authors acknowledge support from NASA grant NNX17AB73G. NVN was partially supported by the NASA AIA contract NNG04EA00C and the NASA STEREO mission under NRL Contract No. N00173-02-C-2035.

Disclosure of Potential Conflicts of Interest The authors declare that they have no conflicts of interest.

References

Billings, D.E.: 1966, *A Guide to the Solar Corona*, Academic Press, New York. ADS.

Bothmer, V., Schwenn, R.: 1998, The structure and origin of magnetic clouds in the solar wind. *Ann. Geophys.* **16**, 1. DOI. ADS.

Cane, H.V., Richardson, I.G.: 2003, Interplanetary coronal mass ejections in the near-Earth solar wind during 1996 – 2002. *J. Geophys. Res.* **108**, 1156. DOI. ADS.

Cheung, M.C.M., Boerner, P., Schrijver, C.J., Testa, P., Chen, F., Peter, H., *et al.*: 2015, Thermal diagnostics with the atmospheric imaging assembly on board the Solar Dynamics Observatory: A validated method for differential emission measure inversions. *Astrophys. J.* **807**, 143. DOI. ADS.

Chi, Y., Shen, C., Wang, Y., Xu, M., Ye, P., Wang, S.: 2016, Statistical study of the interplanetary coronal mass ejections from 1995 to 2015. *Solar Phys.* **291**, 2419. DOI. ADS.

Crooker, N.U., Kahler, S.W., Larson, D.E., Lin, R.P.: 2004, Large-scale magnetic field inversions at sector boundaries. *J. Geophys. Res.* **109**, A03108. DOI. ADS.

D'Huys, E., Seaton, D.B., Poedts, S., Berghmans, D.: 2014, Observational characteristics of coronal mass ejections without low-coronal signatures. *Astrophys. J.* **795**, 49. DOI. ADS.

Echer, E., Gonzalez, W.D., Tsurutani, B.T., Gonzalez, A.L.C.: 2008, Interplanetary conditions causing intense geomagnetic storms (Dst ≤ -100 nT) during solar cycle 23 (1996 – 2006). *J. Geophys. Res.* **113**, A05221. DOI. ADS.

Gosling, J.T.: 1993, The solar flare myth. *J. Geophys. Res.* **98**, 18937. DOI. ADS.

Hess, P., Zhang, J.: 2017, A study of the Earth-affecting CMEs of Solar Cycle 24. *Solar Phys.* **292**, 80. DOI. ADS.

Howard, T.A., Harrison, R.A.: 2013, Stealth coronal mass ejections: A perspective. *Solar Phys.* **285**, 269. DOI. ADS.

Howard, R.A., Michels, D.J., Sheeley, N.R. Jr., Koomen, M.J.: 1982, The observation of a coronal transient directed at Earth. *Astrophys. J. Lett.* **263**, L101. DOI. ADS.

Howard, R.A., Sheeley, N.R. Jr., Michels, D.J., Koomen, M.J.: 1985, Coronal mass ejections – 1979 – 1981. *J. Geophys. Res.* **90**, 8173. DOI. ADS.

Howard, R.A., Moses, J.D., Vourlidas, A., Newmark, J.S., Socker, D.G., Plunkett, S.P., *et al.*: 2008, Sun Earth Connection Coronal and Heliospheric Investigation (SECCHI). *Space Sci. Rev.* **136**, 67. DOI. ADS.

Hudson, H.S., Cliver, E.W.: 2001, Observing coronal mass ejections without coronagraphs. *J. Geophys. Res.* **106**, 25199. DOI. ADS.

Kaiser, M.L., Kucera, T.A., Davila, J.M., St. Cyr, O.C., Guhathakurta, M., Christian, E.: 2008, The STEREO mission: An introduction. *Space Sci. Rev.* **136**, 5. DOI. ADS.

Kilpua, E.K.J., Mierla, M., Zhukov, A.N., Rodriguez, L., Vourlidas, A., Wood, B.: 2014, Solar sources of interplanetary coronal mass ejections during the Solar Cycle 23/24 minimum. *Solar Phys.* **289**, 3773. DOI. ADS.

Kurita, S., Miyoshi, Y., Blake, J.B., Reeves, G.D., Kletzing, C.A.: 2016, Relativistic electron microbursts and variations in trapped MeV electron fluxes during the 8 – 9 October 2012 storm: SAMPEX and Van Allen probes observations. *Geophys. Res. Lett.* **43**, 3017. DOI. ADS.

Lemen, J.R., Duncan, D.W., Edwards, C.G., Friedlaender, F.M., Jurcevich, B.K., Morrison, M.D., *et al.*: 2004, The solar X-ray imager for GOES. In: Fineschi, S., Gummin, M.A. (eds.) *Telescopes and Instrumentation for Solar Astrophysics*, *SPIE CS* **5171**, 65. DOI. ADS.

Lemen, J.R., Title, A.M., Akin, D.J., Boerner, P.F., Chou, C., Drake, J.F., *et al.*: 2012, The Atmospheric Imaging Assembly (AIA) on the Solar Dynamics Observatory (SDO). *Solar Phys.* **275**, 17. DOI. ADS.

Liu, Y.D., Hu, H., Wang, C., Luhmann, J.G., Richardson, J.D., Yang, Z., *et al.*: 2016, On Sun-to-Earth propagation of coronal mass ejections: II. Slow events and comparison with others. *Astrophys. J. Suppl.* **222**, 23. DOI. ADS.

Lugaz, N., Downs, C., Shibata, K., Roussev, I.I., Asai, A., Gombosi, T.I.: 2011, Numerical investigation of a coronal mass ejection from an anemone active region: Reconnection and deflection of the 2005 August 22 eruption. *Astrophys. J.* **738**, 127. DOI. ADS.

Lynch, B.J., Li, Y., Thernisien, A.F.R., Robbrecht, E., Fisher, G.H., Luhmann, J.G., *et al.*: 2010, Sun to 1 AU propagation and evolution of a slow streamer-blowout coronal mass ejection. *J. Geophys. Res.* **115**, A07106. DOI. ADS.

Lynch, B.J., Masson, S., Li, Y., DeVore, C.R., Luhmann, J.G., Antiochos, S.K., *et al.*: 2016, Amodel for stealth coronalmass ejections. *J. Geophys. Res.* **121**, 10677. DOI. ADS.

Ma, S., Attrill, G.D.R., Golub, L., Lin, J.: 2010, Statistical study of coronal mass ejections with and without distinct low coronal signatures. *Astrophys. J.* **722**, 289. DOI. ADS.

Marubashi, K.: 1997, Interplanetary magnetic flux ropes and solar filaments. In: Crooker, N., Joselyn, J.A., Feynman, J. (eds.) *Coronal Mass Ejections*, *Geophys. Monogr. Ser.* **51**, 147. DOI. ADS.

Marubashi, K., Cho, K.-S., Ishibashi, H.: 2017, Interplanetary magnetic flux rope as agent connecting solar eruptions and geomagnetic activities. *Solar Phys.*.

Masson, S., Antiochos, S.K., DeVore, C.R.: 2013, A model for the escape of solar-flare-accelerated particles. *Astrophys. J.* **771**, 82. DOI. ADS.

Mulligan, T., Russell, C.T., Luhmann, J.G.: 1998, Solar cycle evolution of the structure of magnetic clouds in the inner heliosphere. *Geophys. Res. Lett.* **25**, 2959. DOI. ADS.

Nieves-Chinchilla, T., Vourlidas, A., Stenborg, G., Savani, N.P., Koval, A., Szabo, A., *et al.*: 2013, Inner heliospheric evolution of a "stealth" CME derived from multi-view imaging and multipoint in situ observations. I. Propagation to 1 AU. *Astrophys. J.* **779**, 55. DOI. ADS.

Nieves-Chinchilla, T., Vourlidas, A., Raymond, J.C., Linton, M.G., Al-haddad, N., Savani, N.P.,*et al.*: 2017, Understanding the internal magnetic field configuration of ICMEs using 20+ years of Wind observations. *Solar Phys.*, submitted.

Nitta, N.V., DeRosa, M.L.: 2008, A comparison of solar open field regions found by type III radio bursts and the potential field source surface model. *Astrophys. J. Lett.* **673**, L207. DOI. ADS.

Nitta, N.V., Aschwanden, M.J., Freeland, S.L., Lemen, J.R., Wülser, J.-P., Zarro, D.M.: 2014, The association of solar flares with coronal mass ejections during the extended solar minimum. *Solar Phys.* **289**, 1257. DOI. ADS.

Pesnell, W.D., Thompson, B.J., Chamberlin, P.C.: 2012, The Solar Dynamics Observatory (SDO). *Solar Phys.* **275**, 3. DOI. ADS.

Pevtsov, A.A., Panasenco, O., Martin, S.F.: 2012, Coronal mass ejections from magnetic systems encompassing filament channels without filaments. *Solar Phys.* **277**, 185. DOI. ADS.

Reeves, G.D., Spence, H.E., Henderson, M.G., Morley, S.K., Friedel, R.H.W., Funsten, H.O., *et al.*: 2013, Electron acceleration in the heart of the Van Allen radiation belts. *Science* **341**, 991. DOI. ADS.

Richardson, I.G., Cane, H.V.: 2010, Near-Earth interplanetary coronal mass ejections during solar cycle 23 (1996 – 2009): Catalog and summary of properties. *Solar Phys.* **264**, 189. DOI. ADS.

Richardson, I.G., Webb, D.F., Zhang, J., Berdichevsky, D.B., Biesecker, D.A., Kasper, J.C., *et al.*: 2006, Major geomagnetic storms (Dst ≤ -100 nT) generated by corotating interaction regions. *J. Geophys. Res.* **111**, A07S09. DOI. ADS.

Robbrecht, E., Patsourakos, S., Vourlidas, A.: 2009, No trace left behind: STEREO observation of a coronal mass ejection without low coronal signatures. *Astrophys. J.* **701**, 283. DOI. ADS.

Scherrer, P.H., Schou, J., Bush, R.I., Kosovichev, A.G., Bogart, R.S., Hoeksema, J.T., *et al.*: 2012, The Helioseismic and Magnetic Imager (HMI) investigation for the Solar Dynamics Observatory (SDO). *Solar Phys.* **275**, 207. DOI. ADS.

Schrijver, C.J., DeRosa, M.L.: 2003, Photospheric and heliospheric magnetic fields. *Solar Phys.* **212**, 165. DOI. ADS.

Sheeley, N.R. Jr., Howard, R.A., Koomen, M.J., Michels, D.J., Harvey, J.W., Harvey, K.L.: 1982, Observations of coronal structure during sunspot maximum. *Space Sci. Rev.* **33**, 219. DOI. ADS.

Svestka, Z., Cliver, E.W.: 1992, History and basic characteristics of eruptive flares. In: Svestka, Z., Jackson, B.V., Machado, M.E. (eds.) *IAU Coll. 133: Eruptive Solar Flares*, *Lect. Notes Phys.*, **399**, 1, Springer, Berlin. DOI. ADS.

Thorne, R.M., Li, W., Ni, B., Ma, Q., Bortnik, J., Chen, L., *et al.*: 2013, Rapid local acceleration of relativistic radiation-belt electrons by magnetospheric chorus. *Nature* **504**, 411. DOI. ADS.

Tsurutani, B.T., Lee, Y.T., Gonzalez, W.D., Tang, F.: 1992, Great magnetic storms. *Geophys. Res. Lett.* **19**, 73. DOI. ADS.

UeNo, S., Nagata, S.-i., Kitai, R., Kurokawa, H., Ichimoto, K.: 2004, The development of filter vector magnetographs for the Solar Magnetic Activity Research Telescope (SMART). In: Moorwood, A.F.M., Iye, M. (eds.) *Ground-based Instrumentation for Astronomy*, *SPIE CS* **5492**, 958. DOI. ADS.

van der Holst, B., Manchester, W. IV, Sokolov, I.V., Tóth, G., Gombosi, T.I., DeZeeuw, D., *et al.*: 2009, Breakout coronal mass ejection or streamer blowout: The bugle effect. *Astrophys. J.* **693**, 1178. DOI. ADS.

Vourlidas, A., Colaninno, R., Nieves-Chinchilla, T., Stenborg, G.: 2011, The first observation of a rapidly rotating coronal mass ejection in the middle corona. *Astrophys. J. Lett.* **733**, L23. DOI. ADS.

Wagner, W.J.: 1984, Spontaneous coronal mass ejections. *Bull. Amer. Astron. Soc.* **16**, 536. ADS.

Wang, Y., Chen, C., Gui, B., Shen, C., Ye, P., Wang, S.: 2011, Statistical study of coronal mass ejection source locations: Understanding CMEs viewed in coronagraphs. *J. Geophys. Res.* **116**, A04104. DOI. ADS.

Webb, D.F., Nitta, N.V.: 2017, Study on understanding problem forecasts of ISEST campaign flare-CME events. *Solar Phys.*, in press.

Webb, D.F., Cliver, E.W., Crooker, N.U., Cry, O.C.S., Thompson, B.J.: 2000, Relationship of halo coronal mass ejections, magnetic clouds, and magnetic storms. *J. Geophys. Res.* **105**, 7491. DOI. ADS.

Zhang, J., Richardson, I.G., Webb, D.F., Gopalswamy, N., Huttunen, E., Kasper, J.C., *et al.*: 2007, Solar and interplanetary sources of major geomagnetic storms ($\mathrm{Dst} \leq -100$ nT) during 1996 – 2005. *J. Geophys. Res.* **112**, A10102. DOI. ADS.

Zurbuchen, T.H., Richardson, I.G.: 2006, In-situ solar wind and magnetic field signatures of interplanetary coronal mass ejections. *Space Sci. Rev.* **123**, 31. DOI. ADS.